PAPER

Check for updates

Ultrahigh thermoelectric performance of Janus α-STe₂ and α-SeTe₂ monolayers†

Gang Liu, [iD] *[a] Aiqing Guo,[a] Fengli Cao,[a] Weiwei Ju, [iD] [a] Zhaowu Wang, [iD] [a] Hui Wang, [iD] [a] Guo-Ling Li [iD] [b] and Zhibin Gao [iD] *[c]

Janus α-STe₂ and α-SeTe₂ monolayers are investigated systematically using first-principles calculations combined with semiclassical Boltzmann transport theory. Janus α-STe₂ and α-SeTe₂ monolayers are indirect semiconductors with band gaps of 1.20 and 0.96 eV, respectively. It is found that they possess ultrahigh figure of merit (ZT) values of 3.9 and 4.4, respectively, at 500 K, much higher than that of the pristine α-Te monolayer (2.8). The higher ZT values originating from Janus structures reduce lattice thermal conductivities remarkably compared with the pristine α-Te monolayer. The much higher phonon anharmonicity in Janus monolayers leads to significantly lower lattice thermal conductivity. It is also found that electronic thermal conductivity can play an important role in thermoelectric efficiency of materials with quite low lattice thermal conductivity. This work suggests the potential applications of Janus α-STe₂ and α-SeTe₂ monolayers as thermoelectric materials and highlights that using a Janus structure is an effective way to enhance thermoelectric performance.

Introduction

During the past several decades, thermoelectric (TE) materials have attracted much attention as they can convert waste heat into useful electrical power directly. Generally, a dimensionless figure of merit ZT can be used to evaluate the conversion efficiency, which can be expressed as $ZT = S^2\sigma T/(\kappa_e + \kappa_L)$, where S, σ, T, κ_e and κ_L are the Seebeck coefficient, electrical conductivity, absolute temperature, electronic thermal conductivity, and lattice thermal conductivity, respectively. Moreover, $S^2\sigma$ is the power factor (PF). A high ZT value requires a high $S^2\sigma$ and low thermal conductivity ($\kappa_e + \kappa_L$). Unfortunately, the parameters which determine the ZT value are usually interrelated. For instance, S and σ generally behave in an opposite manner, greatly complicating the optimization of ZT values.[1–3] Usually, for a TE material to show excellent electronic transport properties it should possess a narrow band gap.[4,5] However, it has been reported recently that materials with wide band gaps can also have excellent TE performance due to high motilities and low lattice thermal conductivities.[6–8] Various theoretical and

experimental investigations suggest that reducing the dimensionality can improve the ZT value of the TE materials because of the quantum confinement effect and the interface/surface scattering effect.[9–12]

Since the successful exfoliation of graphene in 2004,[13,14] a new field in the study of two-dimensional (2D) materials has opened up. Numerous 2D materials have been investigated theoretically and experimentally for their unique physical and chemical properties.[15–22] Recently, motivated by the successful synthesis of tellurene (2D tellurium),[22] the 2D materials of group VI have attracted much attention, and various 2D materials of Te and Se have been synthesized experimentally.[22–28] It is found that tellurene possesses a high carrier mobility on the order of 10^3 cm² V⁻¹ s⁻¹,[22] outstanding air stability,[29] and a high on/off ratio on the order of 10^6,[24] leading to its potential applications in field-effect transistors (FETs), photodetectors, and sensors. Extraordinary electronic transport properties have also been found for few-layer tellurene.[24,30,31] Furthermore, it also shows good potential applications for thermoelectric devices with high thermoelectric performance.[11,32,33]

Recently, Janus 2D materials have become a research hot spot due to the mirror asymmetry in their structure and the resulting distinct properties. Janus transition metal dichalcogenides (TMDs) have been investigated theoretically and experimentally.[34–37] Investigations suggest that Janus monolayers have promising applications in various fields such as electronics, optoelectronics, photocatalysts, and gas sensing.[38–41] In addition, theoretical research studies have found that Janus monolayers usually reduce κ_L obviously compared with the

[a] *School of Physics and Engineering, Henan University of Science and Technology, Luoyang 471023, People's Republic of China. E-mail: liugang8105@haust.edu.cn*

[b] *Chemistry and Chemical Engineering Guangdong Laboratory, Shantou 515063, People's Republic of China*

[c] *State Key Laboratory for Mechanical Behavior of Materials, Xi'an Jiaotong University, Xi'an 710049, People's Republic of China. E-mail: zhibin.gao@xjtu.edu.cn*

† Electronic supplementary information (ESI) available. See DOI: https://doi.org/10.1039/d2cp03659b

This journal is © the Owner Societies 2022

Phys. Chem. Chem. Phys., 2022, **24**, 28295–28305 | **28295**

pristine monolayers, such as Janus MoSSe, ZrSSe, PtSSe, and SnSSe.[42–45] Thus, the Janus structure may possess higher ZT than the pristine material due to its low thermal conductivity.[46]

In this work, we have investigated the TE properties of Janus α-STe$_2$ and α-SeTe$_2$ monolayers based on the first-principles calculations. For comparison, the pristine α-Te monolayer was investigated as well. The dynamic and thermal stability is confirmed using phonon dispersion and the *ab initio* molecular dynamics (AIMD) simulations. It is found that Janus α-STe$_2$ and α-SeTe$_2$ monolayers possess ultra-high ZT values up to about 4.0 at 500 K, much higher than the maximum ZT value of about 2.8 for α-Te. The ultra-high ZT originates from the good electronic transport properties and ultra-low thermal conductivity. Janus structures reduce the electronic transport properties as the breaking of inversion symmetry but impair κ_L significantly, leading to the enhancement of ZT. Furthermore, the importance of electronic thermal conductivity in TE efficiency is highlighted. The physical mechanisms of low κ_L are also investigated. It is found that much higher phonon anharmonicity results in a lower κ_L in Janus monolayers. And the broken inversion symmetry leads to a higher phonon anharmonicity in Janus monolayers, hence a lower κ_L.

Computational methods

Based on density functional theory (DFT), all the first-principles calculations were performed using the Vienna *ab initio* simulation package (VASP).[47,48] The Perdew–Burke–Ernzerhof (PBE) generalized gradient approximation (GGA) was used as the exchange–correlation functional.[49] For structure optimization, a plane-wave kinetic energy cutoff of 600 eV was chosen, which is much higher than the maximum recommended cutoff to ensure the good convergence of the calculations. During the optimization, a total energy convergence criterion of 10^{-8} eV was chosen, while the force convergence criterion was 10^{-4} eV/Å. A Monkhorst–Pack[50] k-mesh of $15 \times 15 \times 1$ was used to sample the Brillouin zone (BZ). The van der Waals (vdW)

correction proposed by Grimme[51] was taken into consideration during the calculations. The effect of spin–orbit coupling (SOC) was also included due to the presence of heavy elements. As the band gap is always underestimated with PBE, HSE06[52] was employed to obtain an accurate electronic band structure and density of states (DOS). To verify the thermal stability, the *ab initio* molecular dynamics (AIMD) simulations controlled using a Nose–Hoover thermostat[53,54] have been performed for 5000 fs with a time step of 1 fs. The electronic transport properties are implemented in the BoltzTraP2 code,[55] where Boltzmann transport theory and relaxation time approximation (RTA) are utilized. The phonon dispersions were obtained using Phonopy.[56] The AlmaBTE code was used to calculate the lattice thermal conductivity by solving the Boltzmann transport equation.[57]

Results and discussion

The structure of the α-Te monolayer belongs to the $\bar{P}3M1$ (164) symmetry group, similar to that of 1T-MoS$_2$. The Janus monolayers are built from the pristine α-Te by replacing Te atoms of the outer layer with S/Se atoms. The optimized structures of three monolayers are shown in Fig. 1, including α-Te. From the side views, it can be found that the symmetry is broken as two surfaces of the Janus monolayer consist of different chalcogen atoms. The lattice constant a and buckling height d of the optimized structures are listed in Table 1, as well as the cohesive energies E_c per atom for the three materials. Cohesive energy E_c is defined as: $E_c = \dfrac{E_{tot} - (mE_{Se} + nE_{Te})}{m+n}$, where E_{tot} is the total energy of the material studied, while E_{Se} and E_{Te} are those of isolated Se and Te atoms, respectively. Here m and n are the numbers of Se and Te atoms in a primitive cell. The calculated E_c values are -2.38, -2.24, and -2.08 eV for α-STe$_2$, α-SeTe$_2$ and α-Te monolayers, respectively. This indicates the energetic stability of the Janus monolayers. Moreover, the AIMD simulations also confirm the thermal stability of the three monolayers up to 500 K, as shown in Fig. S1 of the ESI.†
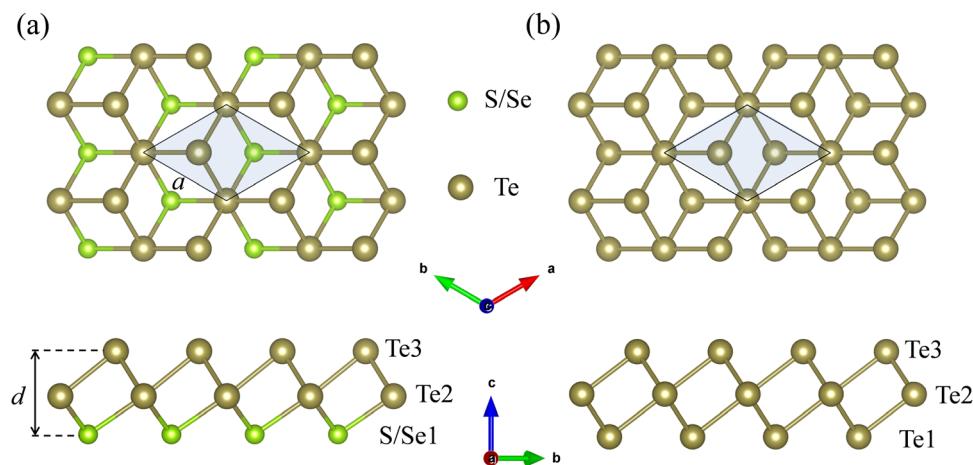

Fig. 1 Side and top views of Janus (a) α-S/SeTe$_2$ and (b) α-Te monolayers. The primitive cells are displayed with blue shading. The symbols S/Se/Te1, Te2, Te3 indicate the atoms located in different layers.

28296 | *Phys. Chem. Chem. Phys.*, 2022, **24**, 28295–28305

This journal is © the Owner Societies 2022

Table 1 Lattice constant a and buckling height d of optimized structures, as well as the cohesive energies E_c per atom

	α-STe$_2$	α-SeTe$_2$	α-Te
a (Å)	4.03	4.05	4.15
d (Å)	3.34	3.49	3.67
E_c (eV)	−2.38	−2.24	−2.08

The electronic band structure plays an important role in TE performance. It should be noted that the HSE06 hybrid functional including SOC effects (HSE + SOC) is necessary for obtaining an accurate band structure of the materials containing heavy elements. For instance, the experimental value of the band gap is about 0.33 eV for bulk Te,[58] while the calculated value is 0.31 eV with the HSE + SOC method,[31] very close to the experimental one. For comparison, the PBE, PBE + SOC, and HSE without SOC methods led to values different from the experimental value remarkably.[31] The band gaps calculated with HSE + SOC, HSE, PBE + SOC, and PBE are listed in Table 2. For α-STe$_2$, α-SeTe$_2$, and α-Te monolayers, the band gaps calculated using HSE + SOC are indirect with values of about 1.22, 0.96, and 0.70 eV, respectively. The data are in good agreement with previous studies.[22,33,59] Furthermore, the band gaps calculated using other methods are significantly different from those calculated using HSE + SOC. For instance, the band gaps calculated using HSE are 1.51, 1.21, and 1.12 eV, significantly larger than those calculated using HSE + SOC. It also verifies that the SOC effect cannot be neglected for the materials containing a heavy Te element. The calculated electronic band structures and partial DOS (PDOS) of the three monolayers with the method of HSE + SOC are shown in Fig. 2, while the band structures calculated using HSE without SOC are shown as well. The conduction band minimum (CBM) is located at the Γ point for all the monolayers. However, the valence band maximum (VBM) is located in the Γ–M line for α-Te, while they are located in the Γ–K line for α-STe$_2$ and α-SeTe$_2$. On the whole, the shapes of band structures are similar, implying that they may have similar values of effective masses overall for three monolayers, as listed in Table 3. However, the VBM of α-Te is located far from the ones of Janus monolayers, resulting in a large difference in $m^\star$ of holes. Moreover, the valence bands near the Fermi level are relatively flat, facilitating a high PF value, similar to those of Na$_x$CoO$_2$ and FeAs$_2$.[60–62] In Fig. 2, it is also found that SOC remarkably affects the shapes of the band structure and the locations of the VBM and CBM. The shapes of curves around the VBM and CBM have a great effect on $m^\star$. Thus, we choose the data of HSE + SOC to obtain an accurate TE performance. From the PDOS, we can find that the atoms of two outer layers (Te1 and Te3) contribute identically due to the inversion symmetry of the structure in α-Te, whereas the contributions of two outer layers (S/Se1 and Te3) are not the same in Janus monolayers. The outer S/Se1 atoms contribute much less than the Te2 atoms in the middle layer in Janus monolayers around the CBM, while the contributions of outer Te1/Te3 atoms are nearly the same as those of the Te2 atoms in α-Te.

The phonon dispersions along high-symmetry lines are investigated, as shown in Fig. 3. The corresponding projected phonon density of states (PhDOS) are also displayed together. There is no negative frequency, indicating the dynamical stability of the three monolayers. In fact, the stabilities of the Janus monolayers were also confirmed in previous studies.[59,63] There are three acoustic phonon branches and six optical phonon branches, as there are three atoms in each primitive cell. The out-of-plane acoustic (ZA), transverse acoustic (TA), and longitudinal acoustic (LA) branches are displayed in red, blue and magenta lines, respectively. Note that the ZA phonon branches are quadratic around the Γ point, while TA and LA branches are linear. It is found that the highest frequencies of α-STe$_2$, α-SeTe$_2$, and α-Te monolayers are 7.59, 6.23, and 5.73 THz, respectively. This mainly results from the fact that α-STe$_2$ has the lowest average atom mass, while that of α-Te is the heaviest. In α-Te, the Te atom of the middle layer dominates the PhDOS in the high-frequency range of 3.5–6.0 THz, while the atom of the outer layers contributes significantly in the low-frequency range. Moreover, the contributions of Te1 and Te3 are identical due to the inversion symmetry of the structure. In Janus monolayers, the lighter S/Se atom contributes much more in the high-frequency range. In particular, the S atom is even dominant in the high-frequency range for α-STe$_2$, as it is much lighter than the Te atom. Note that there is a phonon gap between acoustic and optical phonon modes in α-Te, whereas it does not appear in the two Janus monolayers. Compared to pristine α-Te, the breaking of the symmetry in the Janus monolayers leads to the breaking of degeneracies and obvious splits between phonon branches, such as at the high-symmetry point K.

The vibrating patterns of the nine phonon modes around the Γ point are investigated, as shown in Fig. 4. Note that the mode number is given in the ascending order of phonon frequency. Modes 1 to 3 belong to acoustic phonons, while modes 4 to 9 belong to optical phonons. It is found that modes 4, 5, and 8 of Janus monolayers have significant differences between pristine α-Te monolayers. In α-Te, the vibrations of these modes have inversion symmetry along the c-direction, as the structure is symmetrical. However, as in Janus monolayers, the Te atoms of one outer layer are substituted by S/Se atoms, the inversion symmetry of the structure is broken, hence the symmetry of vibration.

By solving the Boltzmann transport equation with the constant relaxation time and single parabolic band (SPB) model,[64] we investigate the electronic transport coefficients of the three monolayers, including the S, σ, and PF. Two typical temperatures (300 and 500 K) are selected in the calculation, as shown
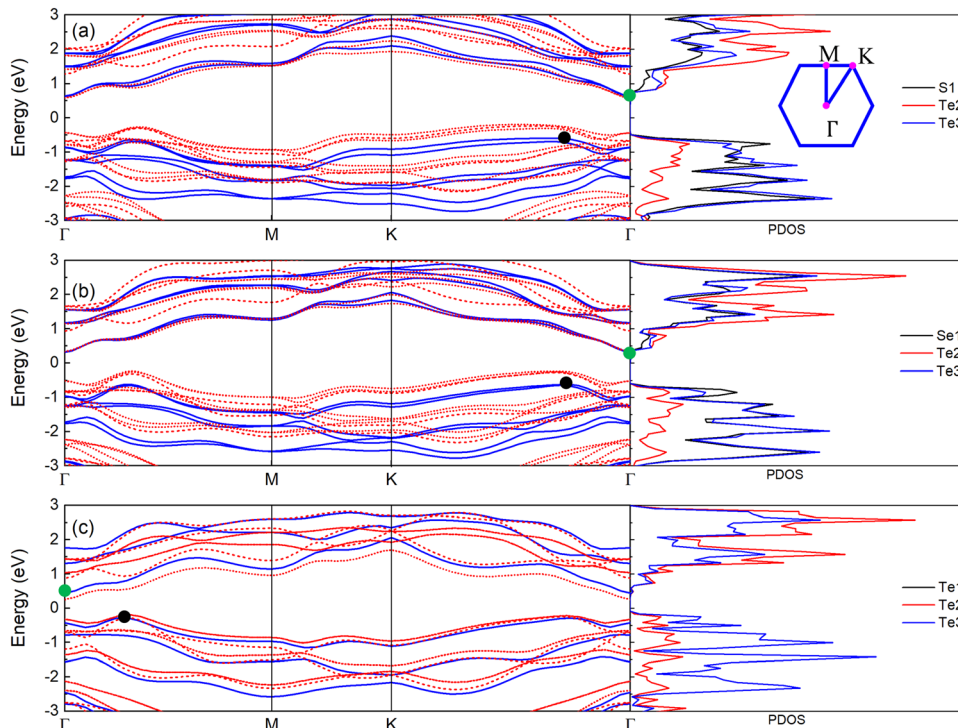
Table 2 Calculated band gaps with HSE + SOC, HSE, PBE + SOC, and PBE for each monolayer

	HSE + SOC (eV)	HSE (eV)	PBE + SOC (eV)	PBE (eV)
α-STe$_2$	1.22	1.51	0.78	1.05
α-SeTe$_2$	0.96	1.21	0.58	0.79
α-Te	0.70	1.12	0.44	0.76

This journal is © the Owner Societies 2022

Phys. Chem. Chem. Phys., 2022, **24**, 28295–28305 | **28297**

Fig. 2 Electronic band structures of Janus (a) α-STe$_2$, (b) α-SeTe$_2$, and (c) pristine α-Te monolayers with HSE + SOC, exhibited by blue solid lines. For comparison, the band structures calculated using HSE without SOC are shown in red dashed lines. The partial phonon density of states (PDOS) are also displayed. The inset shows the chosen high-symmetry points. The green and black circles indicate the locations of the CBM and VBM of HSE + SOC for each monolayer. The symbols S/Se/Te1, Te2, and Te3 represent atoms of different layers, as shown in Fig. 1.

Table 3 Elastic constant C_{2D}, effective mass m^*, DP constant E_i, carrier mobility μ and the carrier relaxation time τ at room temperature. m_e represents the rest mass of the electron

	Carrier type	C$_{2D}$ (N/m)	m^* (m_e)	E_i (ev)	μ (cm^2 V^{-1} S^{-1})	τ (ps)
α-STe$_2$	Electron	50.91	0.125	6.06	1.90×10^3	0.135
	Hole		0.288	3.92	8.52×10^2	0.140
α-SeTe$_2$	Electron	46.49	0.114	6.18	2.00×10^3	0.130
	Hole		0.288	4.36	6.30×10^2	0.103
α-Te	Electron	40.48	0.097	5.86	2.67×10^3	0.148
	Hole		0.189	3.58	1.89×10^3	0.203

in Fig. 5. On the whole, it is found that the absolute values of Seebeck coefficient $|S|$ decrease for all the three monolayers with an increase in the carrier concentration n, as displayed in Fig. 5(a)–(c). Based on the Mahan–Sofo theory,[65] $|S|$ for 2D materials can be expressed using the following simple model:[12]

$$|S| = \frac{2\pi^3 k_B^2}{3eh^2 n} m^* T,\qquad (1)$$

where h, k_B, m^*, and e are the Planck constant, Boltzmann constant, effective mass, and electron charge, respectively. It is found that $|S|$ is proportional to m^*, and inversely proportional to n at a given temperature. From Table 3, it is found that m^* of the holes is much larger than that of the electrons, due to the smaller band curvature around the VBM than that around the CBM as shown in Fig. 2. Thus, $|S|$ of p-type doping is bigger than that of n-type doping for three monolayers. $|S|$ values are

close to each other among the three monolayers. For instance, at 500 K and 10^{13} cm^{-2} of n, $|S|$ values are 323, 331, and 312 μV K^{-1} for α-STe$_2$, α-SeTe$_2$, and α-Te monolayers, respectively. Furthermore, $|S|$ at 500 K is higher than that at 300 K, as it is proportional to T based on eqn (1).

The carrier relaxation time τ is required to obtain σ.[55] From the conventional Boltzmann transport theory, electrical conductivity σ is proportional to the carrier relaxation time τ, which can be expressed as $\tau = \frac{m^* \mu}{e}$, where μ is the carrier mobility. By using the deformation potential (DP) theory, μ of 2D materials can be written as:[66]

$$\mu = \frac{e\hbar^3 C_{2D}}{k_B T m^* m_d E_i^2},\qquad (2)$$

where $\hbar$ and C_{2D} are the reduced Planck constant and 2D elastic constant, respectively. m_d is the average effective mass calculated using $m_d = \sqrt{m_x^* m_y^*}$. However, for in-plane isotropic materials here, $m_x^* = m_y^*$. $E_i = \frac{\Delta E_{edge}}{\Delta a/a}$ is the deformation potential constant, where ΔE_{edge} is the shift in the band energy of the VBM/CBM under small compression or expansion, and Δa is the change in the lattice parameter relative to the equilibrium lattice parameter a. The vacuum energy level correction is considered in the calculations. The calculated data are listed in Table 3. From the α-STe$_2$ to α-Te monolayer, C_{2D} becomes smaller, as the S–Te bond is the strongest and the
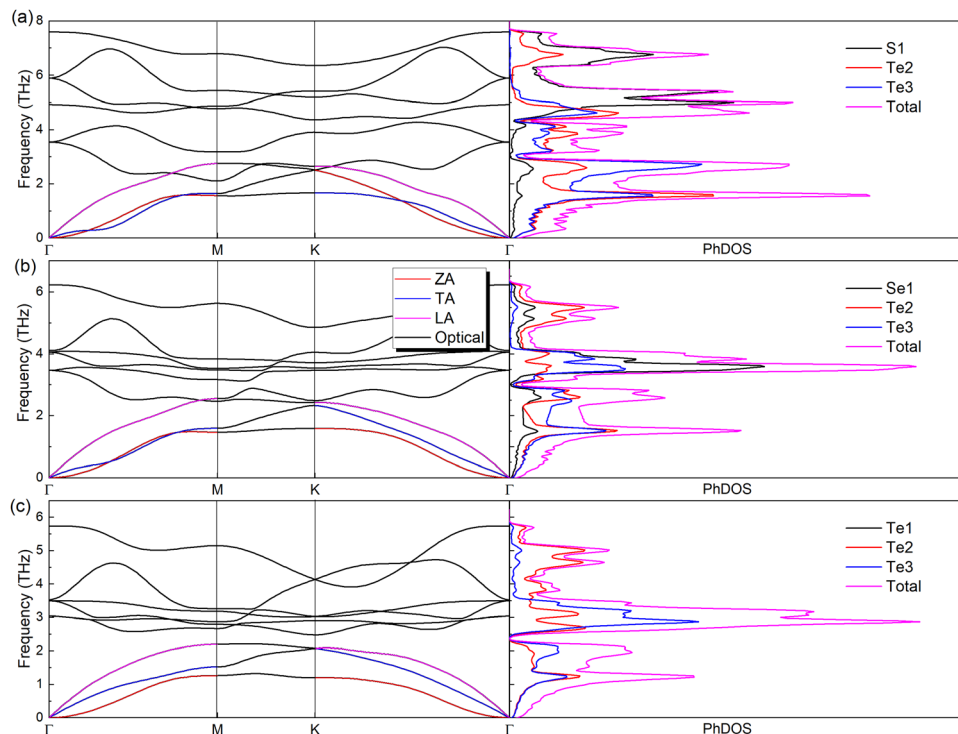
28298 | *Phys. Chem. Chem. Phys.*, 2022, **24**, 28295–28305

This journal is © the Owner Societies 2022

Fig. 3 Phonon dispersions and projected PhDOS of (a) α-STe₂, (b) α-SeTe₂, and (c) α-Te monolayers. Red, blue, and magenta lines indicate ZA, TA, and LA phonon branches, respectively.

Te–Te bond is the weakest. The carrier relaxation times τ of electrons and holes for the three monolayers are close to each other, in the range of 0.1–0.2 ps.

The electrical conductivity σ of the three monolayers is obtained through the calculated carrier relaxation time τ, as shown in Fig. 4(d)–(f). It is found that σ increases with the increasing carrier concentration n, and decreases with

Fig. 4 Vibration patterns of the nine phonon modes around the Γ point for Janus monolayers (a) and pristine α-Te monolayers (b). The arrows show the vibration directions of each atom. The number is given in the ascending order of phonon frequency for each mode.

temperature T. The curves of 300 K are higher than the ones of 500 K. On the whole, σ of n-type doping is higher than that of p-type doping at the same n and T. The dependencies of σ can be interpreted using a simple model $\sigma = ne\mu$.[67] It correlates positively with n, contrary to the situation of S. Furthermore, σ is inversely proportional to m^* and T based on eqn (2). As m^* of an electron is smaller than that of a hole for each monolayer, σ of n-type doping is higher.

Then, based on S and σ, the power factor PF as a function of carrier concentration n is calculated and shown in Fig. 4(g)–(i). A high value of PF needs a large S and σ simultaneously, as PF $= S^2\sigma$. PF has a maximum value at an optimum n, due to the decreasing function of S and the increasing function of σ. In all cases, the PF value of n-type and p-type doping increases first and then decreases with increasing n. It is found that PF values at 300 K are generally higher than the values at 500 K for n-type and p-type doping. Moreover, the PF values of n-type doping are much lower than those of p-type doping for the three monolayers. The maximum values of PF are 0.035, 0.034, and 0.055 W mK^{-2} for p-type doped α-STe₂, α-SeTe₂, and α-Te monolayers, respectively, at 300 K. At 500 K, the maximum values are 0.036, 0.028, and 0.040 W mK^{-2}, respectively. The high values of PF are comparable with those of many TE materials, such as 2D SnSe and Penta-silicene,[12,68] indicating they may show high TE performance as well.

A high value of ZT also needs a minimum thermal conductivity, including electronic thermal conductivity κ_e and lattice thermal conductivity κ_L. κ_e can be calculated through the Wiedemann–Franz law: $\kappa_e = L\sigma T$, where L is the Lorenz number.[69]
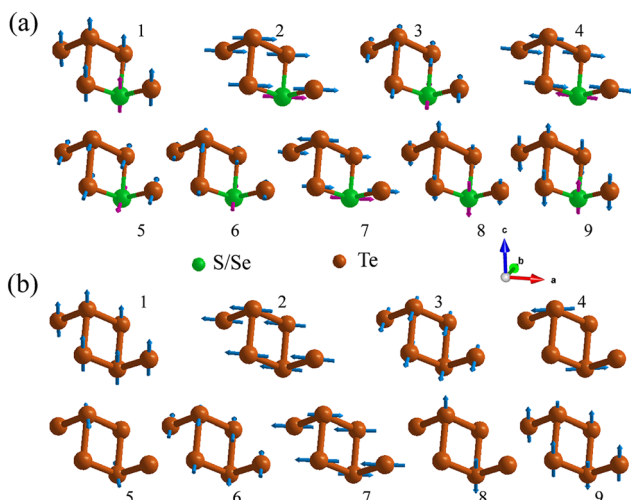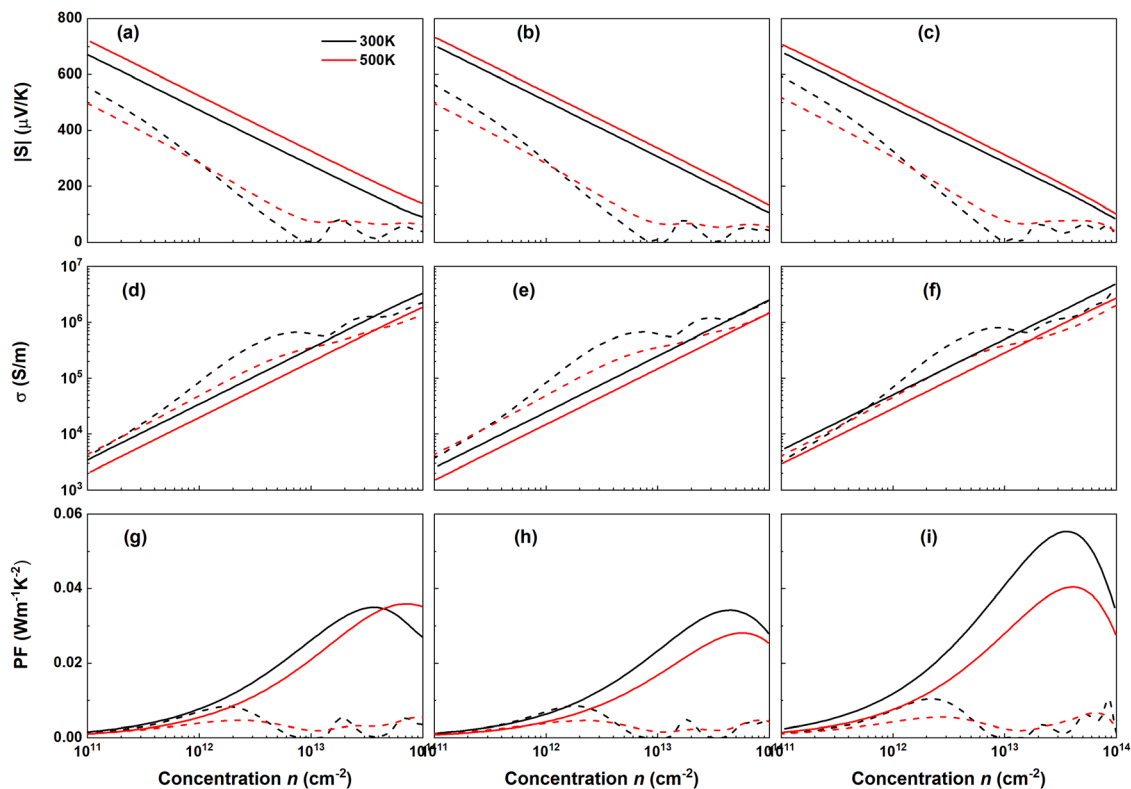
This journal is © the Owner Societies 2022

Phys. Chem. Chem. Phys., 2022, **24**, 28295–28305 | **28299**

Fig. 5 Concentration n dependencies of $|S|$, σ, and PF at 300 and 500 K for the three monolayers. The solid lines indicate the data of p-type doping, while the dashed lines represent n-type doping. And the 1st, 2nd and 3rd columns correspond to the Janus α-STe$_2$, α-SeTe$_2$, and pristine α-Te monolayers, respectively.

The calculated κ_e values of the three monolayers at 300 and 500 K are displayed in Fig. 6. Since κ_e and σ are linearly related, κ_e shows similar dependencies on n and m^*. κ_e is very small when n is lower than 10^{13} cm^{-2}, whereas it increases sharply and exceeds 15 Wm^{-1} K^{-1} at 10^{14} cm^{-2}. On the whole, κ_e is much larger for n-type doping than for p-type doping
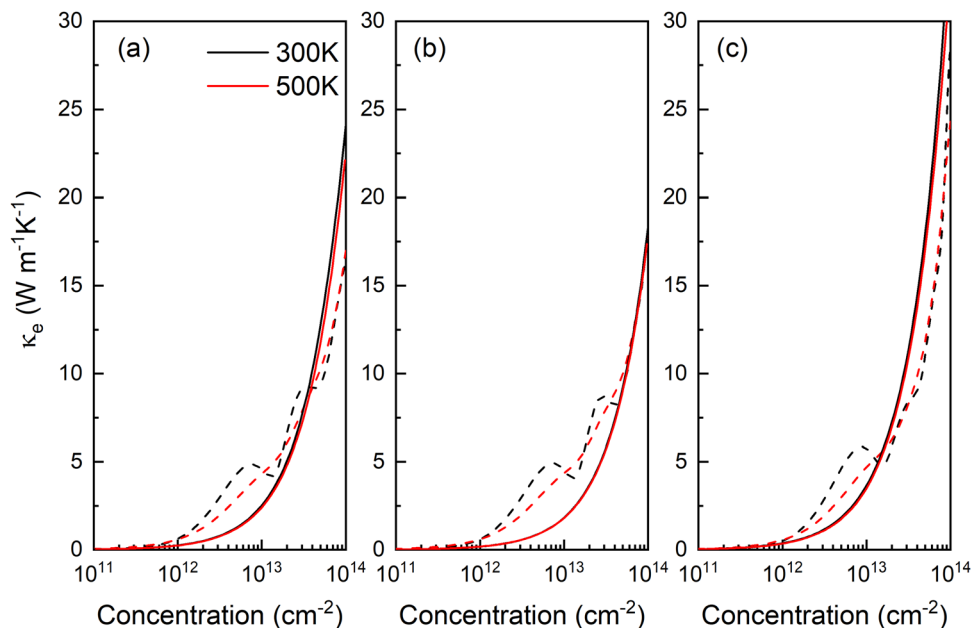

Fig. 6 Electronic thermal conductivity κ_e of (a) α-STe$_2$, (b) α-SeTe$_2$, and (c) α-Te monolayers at 300 and 500 K. Solid lines indicate κ_e of p-type doping, while dashed lines indicate the ones of n-type doping.

28300 | *Phys. Chem. Chem. Phys.*, 2022, **24**, 28295–28305

This journal is © the Owner Societies 2022

when n is lower than 10^{13} cm^{-2}, as $m^\star$ of the electrons is lower than that of the holes. Combined with lower PF, the ZT value of n-type doping should be much smaller than that of p-type doping. As the $m^\star$ of a hole in the α-Te monolayer is the lowest among the three monolayers, κ_e of the α-Te monolayer is the largest. For instance, κ_e values are 1.30, 0.89, and 1.82 Wm^{-1} K^{-1} for p-type doped α-STe$_2$, α-SeTe$_2$, and α-Te monolayers, respectively, at 300 K, 5 × 10^{12} cm^{-2}. It is also found that κ_e is independent of T approximately.

The κ_L values of full solution for the α-STe$_2$, α-SeTe$_2$, and α-Te monolayers are calculated, as shown in Fig. 7. For comparison, the values obtained by the relaxation time approximation (RTA) approach are also displayed. To calculate the κ_L of 2D materials, an effective thickness is required, which can be defined as the summation of the buckling height h and the van der Waals radii of the atoms of the outer layer.[70] The effective thicknesses are 7.20, 7.45, and 7.79 Å for α-STe$_2$, α-SeTe$_2$, and α-Te monolayers, respectively. The ultralow values of κ_L obtained from the full solution (RTA) are 1.18 (0.39), 0.73 (0.32), and 3.01 (1.12) Wm^{-1} K^{-1} at 300 K, respectively. Although the RTA approach underestimates κ_L significantly, it is particularly useful for a quite big sample size and slow heating experimental conditions.[71–73] However, our discussion is based on the results of full solution, as our work focuses more on the theoretical research. The values are in agreement with those of previous studies.[33,59] The κ_L values are much lower than those of many 2D monolayers, such as graphene (3716 Wm^{-1} K^{-1}),[74,75] silicene (28.3 Wm^{-1} K^{-1}),[74,75] blue phosphorene (106.6 Wm^{-1} K^{-1}),[74] and MoS$_2$ monolayers (87.6 Wm^{-1} K^{-1}).[76] An ultralow κ_L value generally corresponds to high TE efficiency. It is also found that κ_L values are close to κ_e at 5 × 10^{12} cm^{-2} and room temperature. As is well known, κ_L usually dominates the TE performance, while the effect of κ_e can be neglected. However, κ_e is comparable to κ_L here, as κ_L is quite low (around 1 Wm^{-1} K^{-1}). It implies that κ_e may also play
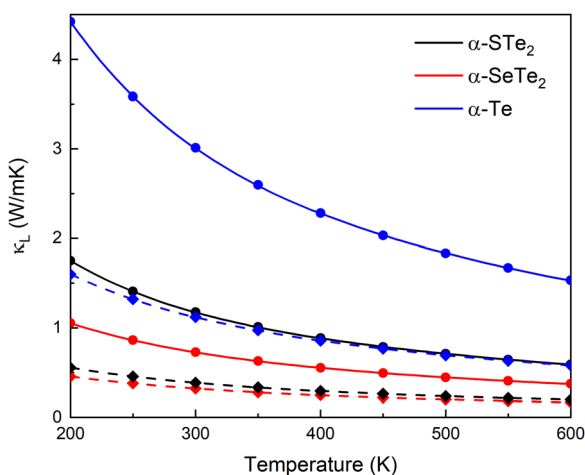
Table 4 Normalized contribution of each phonon mode to the total κ_L for the three 2D materials. The mode number is given in the ascending order of phonon frequency around the Γ point. Modes 1 to 3 belongs to the acoustic mode, and the others belong to the optical mode

Mode	1	2	3	4	5	6	7	8	9
α-STe$_2$	0.267	0.260	0.148	0.073	0.118	0.016	0.011	0.095	0.012
α-SeTe$_2$	0.145	0.140	0.137	0.076	0.027	0.020	0.039	0.324	0.092
α-Te	0.156	0.230	0.192	0.021	0.005	0.031	0.016	0.262	0.087

an important role in TE performance. Furthermore, the curves of κ_L well satisfy the relationship $\kappa_L \propto 1/T$, indicating the dominant Umklapp process. At 500 K, κ_L values are reduced to 0.71, 0.45, and 1.83 Wm^{-1} K^{-1} for α-STe$_2$, α-SeTe$_2$, and α-Te monolayers, respectively.

Furthermore, the normalized contribution of each mode to total κ_L at 300 K is also investigated, as listed in Table 4. It is found that the acoustic modes contribute 67.5%, 42.1% and 57.8% to the total κ_L for α-STe$_2$, α-SeTe$_2$, and α-Te monolayers, respectively. In other words, the contributions of optical modes are 32.5%, 57.9%, and 42.2%, respectively. The contributions of optical phonons are quite significant, much higher than those of many other 2D materials, such as graphene,[77] MoS$_2$ monolayer,[76] and stanene.[78]

Debye temperature Θ_D is related closely to the thermal properties of materials, and can be expressed as $\Theta_D = h\omega_{max}/k_B$, where h and ω_{max} are the Planck constant and the maximum of acoustic phonon frequency, respectively.[79] They are 131, 123, and 105 K for α-STe$_2$, α-SeTe$_2$, and α-Te monolayers, respectively. Usually, high Θ_D indicates strong harmonic properties, and hence high κ_L. However, α-Te possesses the lowest Θ_D and the highest κ_L among the three monolayers. The abnormal case of κ_L stems from Θ_D measures the harmonic properties only, whereas κ_L is determined by both harmonic and anharmonic properties. To unveil the underlying physical mechanisms, the total phase space for three-phonon processes P_3 and Grüneisen parameters γ are calculated, as displayed in Fig. 8. Note that P_3 is the direct measure of the number of scattering processes available to each phonon, depending on the phonon dispersions only.[75,80] Based on Fig. 8(a)–(c) the dispersions of P_3 are similar to each other, indicating that they are not the main reason for the abnormal κ_L of the monolayers. On the other hand, the Grüneisen parameter γ is the measure of the anharmonic interactions, and a high value of γ leads to a low κ_L.[75,81] Overall, $|\gamma|$ of α-Te is smaller than those of α-STe$_2$ and α-SeTe$_2$, as shown in Fig. 8(d)–(f), especially for the TA phonon branch. Specifically, the maximum value of $|\gamma|$ is only 2.6 for α-Te, while it can reach 20 for α-STe$_2$ and α-SeTe$_2$. The phonon relaxation times τ_{ph} of the three monolayers are also exhibited in Fig. 8(g)–(i). τ_{ph} of α-STe$_2$ and α-SeTe$_2$ is significantly lower than that of α-Te, resulting from the much higher $|\gamma|$. It is concluded that due to the breaking of the inversion symmetry with respect to the central plane of the structure, the Janus α-STe$_2$ and α-SeTe$_2$ monolayers introduce much stronger anharmonicity, leading to an abnormally lower κ_L than that of α-Te.[45]

Based on the electronic and thermal transport coefficients, the ZT values of the three monolayers are estimated and shown

Fig. 7 Temperature dependence of lattice thermal conductivity κ_L for α-STe$_2$, α-SeTe$_2$, and α-Te monolayers. The circles represent the values of κ_L obtained from the full solution, while the solid lines indicate the corresponding 1/T fitting. For comparison, the diamonds and dashed lines represent the data of the RTA approach.
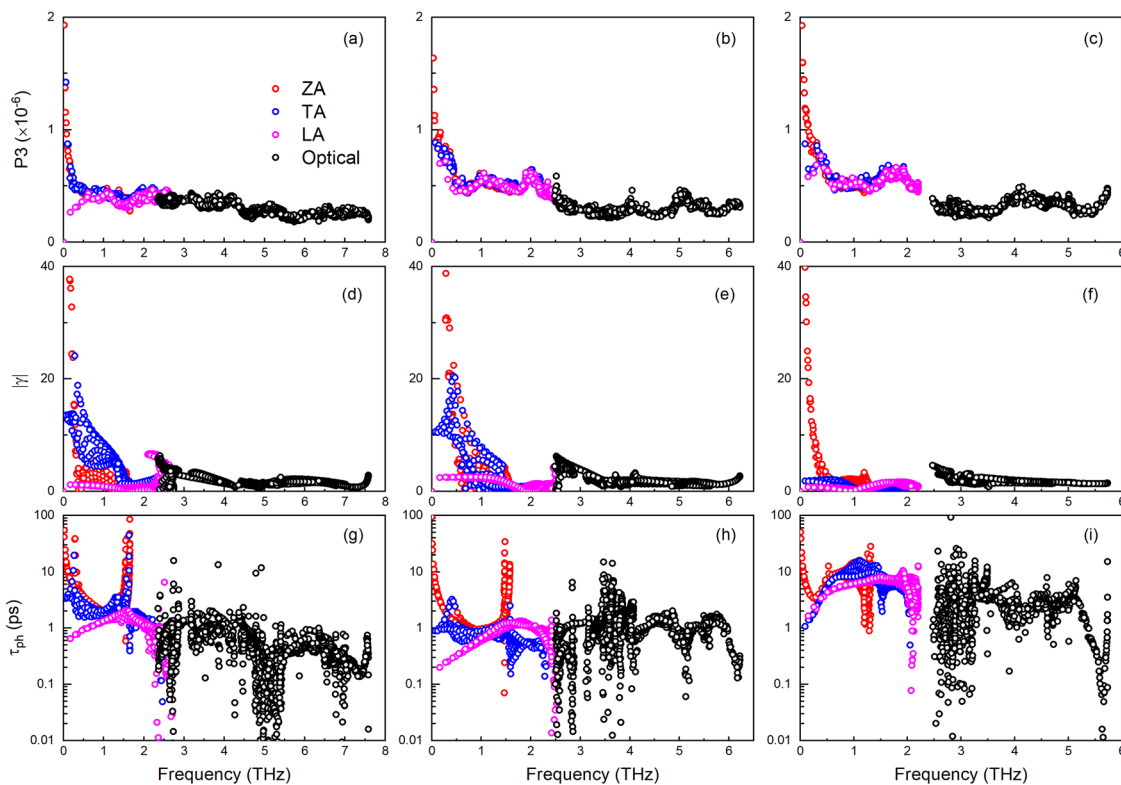
Fig. 8 (a–c) Total phase space for three-phonon processes P_3, (d–f) absolute value of Grüneisen parameters $|\gamma|$, and (g–i) phonon relaxation time τ_{ph} for the three monolayers. Note that the 1st, 2nd and 3rd columns correspond to the Janus α-STe$_2$, α-SeTe$_2$ and α-Te monolayers, respectively.
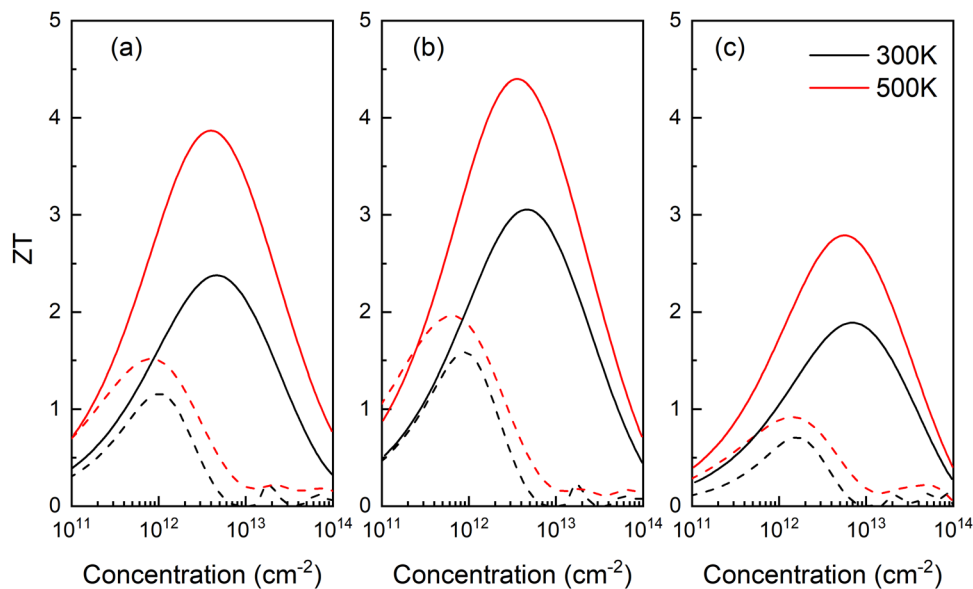

Fig. 9 Figure of merit ZT for (a) Janus α-STe$_2$, (b) α-SeTe$_2$ and (c) pristine α-Te monolayers, respectively. The solid lines indicate the values of p-type doped monolayers, while the dashed lines represent the n-type doping.

in Fig. 9. They possess ultrahigh ZT values for p-type doping. At 500 K, the three monolayers have the maximum ZT values of 3.9, 4.4, and 2.8 for α-STe$_2$, α-SeTe$_2$ and α-Te monolayers, respectively, corresponding to the values of n of 4×10^{12}, 4×10^{12}, and 5×10^{12} cm^{-2}. The α-SeTe$_2$ monolayer has the

highest ZT value as it has the lowest κ_e and κ_L (0.67 and 0.45 Wm^{-1} K^{-1}) at 500 K, while the ones of pristine α-Te are the highest (1.95 and 1.83 Wm^{-1} K^{-1}). Therefore, the much lower κ_L of the α-SeTe$_2$ monolayer mainly leads to a much higher ZT value than that of α-Te. For the three monolayers

28302 | *Phys. Chem. Chem. Phys.*, 2022, **24**, 28295–28305

This journal is © the Owner Societies 2022

studied here, higher PF does not always lead to higher ZT. For example, α-Te has the highest PF (0.040 Wm^{-1} K^{-2} at 500 K) and the lowest ZT, whereas α-SeTe$_2$ possesses the lowest PF (0.028 Wm^{-1} K^{-2} at 500 K) and the highest ZT. Thus, it can be concluded that Janus structures can enhance TE performance remarkably as they have much lower thermal conductivity, including κ_e and κ_L. Additionally, it is also found that κ_e is a little higher than κ_L in the three monolayers, and can affect ZT significantly. It confirms that κ_e cannot be neglected for the TE materials with quite low κ_L. Even at room temperature, these monolayers also have large ZT values, which reach 2.4, 3.1, and 1.9 for α-STe$_2$, α-SeTe$_2$ and α-Te, respectively. Thus, these materials are especially suitable for TE devices in daily life. On the other hand, the ZT values are much lower for n-type doping than for p-type, because of the smaller PF values and larger κ_e values for n-type doping.

Conclusions

In summary, the electronic, thermal transport properties and TE performances of Janus α-STe$_2$ and α-SeTe$_2$ monolayers are investigated using first-principles calculations combined with semiclassical Boltzmann theory. For comparison, the TE properties of the pristine α-Te monolayer are also studied. The electronic band structures, effective masses, and carrier relaxation times are similar to each other. Janus structures have different VBM, larger band gaps, and reduced PF values, compared with the pristine α-Te. However, the breaking of the inversion symmetry greatly reduces the κ_L by enhancing the phonon anharmonicity in the Janus α-STe$_2$ and α-SeTe$_2$ monolayers. Furthermore, Janus monolayers also possess smaller κ_e. Note here that κ_e plays an important role in ZT as it can be comparable with κ_L. Thus, the ZT values of the Janus α-STe$_2$ and α-SeTe$_2$ monolayers are much higher than those of the pristine α-Te monolayer. Particularly, the ZT value of the Janus α-SeTe$_2$ monolayer is as high as about 4.4 at 500 K. Our work indicates that Janus α-SeTe$_2$ and α-STe$_2$ are promising thermoelectric materials. Furthermore, it also suggests that using a Janus structure is an effective method to reduce κ_L and enhance ZT.

Conflicts of interest

There are no conflicts to declare.

Acknowledgements

References

1 W. Liu, X. Yan, G. Chen and Z. Ren, *Nano Energy*, 2012, **1**, 42–56.

2 J. Yang, L. Xi, W. Qiu, L. Wu, X. Shi, L. Chen, J. Yang, W. Zhang, C. Uher and D. J. Singh, *npj Comput. Mater.*, 2016, **2**, 15015.

3 T. Zhu, Y. Liu, C. Fu, J. P. Heremans, J. G. Snyder and X. Zhao, *Adv. Mater.*, 2017, **29**, 1605884.

4 K. Biswas, J. He, I. D. Blum, C.-I. Wu, T. P. Hogan, D. N. Seidman, V. P. Dravid and M. G. Kanatzidis, *Nature*, 2012, **489**, 414–418.

5 C. M. Jaworski, B. Wiendlocha, V. Jovovic and J. P. Heremans, *Energy Environ. Sci.*, 2011, **4**, 4155–4162.

6 X. Su, N. Zhao, S. Hao, C. C. Stoumpos, M. Liu, H. Chen, H. Xie, Q. Zhang, C. Wolverton, X. Tang and M. G. Kanatzidis, *Adv. Funct. Mater.*, 2019, **29**, 1806534.

7 C. Xiao, K. Li, J. Zhang, W. Tong, Y. Liu, Z. Li, P. Huang, B. Pan, H. Su and Y. Xie, *Mater. Horiz.*, 2014, **1**, 81–86.

8 N. Wang, M. Li, H. Xiao, Z. Gao, Z. Liu, X. Zu, S. Li and L. Qiao, *npj Comput. Mater.*, 2021, **7**, 18.

9 M. S. Dresselhaus, G. Chen, M. Y. Tang, R. G. Yang, H. Lee, D. Z. Wang, Z. F. Ren, J. P. Fleurial and P. Gogna, *Adv. Mater.*, 2007, **19**, 1043–1053.

10 R. Venkatasubramanian, E. Siivola, T. Colpitts and B. O'Quinn, *Nature*, 2001, **413**, 597–602.

11 Z. Gao, G. Liu and J. Ren, *ACS Appl. Mater. Interfaces*, 2018, **10**, 40702–40709.

12 Z. Gao and J. S. Wang, *ACS Appl. Mater. Interfaces*, 2020, **12**, 14298–14307.

13 K. S. Novoselov, A. K. Geim, S. V. Morozov, D. Jiang, Y. Zhang, S. V. Dubonos, I. V. Grigorieva and A. A. Firsov, *Science*, 2004, **306**, 666–669.

14 S. Stankovich, D. A. Dikin, R. D. Piner, K. A. Kohlhaas, A. Kleinhammes, Y. Jia, Y. Wu, S. T. Nguyen and R. S. Ruoff, *Carbon*, 2007, **45**, 1558–1565.

15 A. H. C. Neto and K. Novoselov, *Rep. Prog. Phys.*, 2011, **74**, 082501.

16 K. F. Mak, C. Lee, J. Hone, J. Shan and T. F. Heinz, *Phys. Rev. Lett.*, 2010, **105**, 136805.

17 A. Splendiani, L. Sun, Y. Zhang, T. Li, J. Kim, C.-Y. Chim, G. Galli and F. Wang, *Nano Lett.*, 2010, **10**, 1271–1275.

18 L. Li, Y. Yu, G. J. Ye, Q. Ge, X. Ou, H. Wu, D. Feng, X. H. Chen and Y. Zhang, *Nat. Nanotechnol.*, 2014, **9**, 372–377.

19 C. Zhi, Y. Bando, C. Tang, H. Kuwahara and D. Golberg, *Adv. Mater.*, 2009, **21**, 2889–2893.

20 S. Z. Butler, S. M. Hollen, L. Cao, Y. Cui, J. A. Gupta, H. R. Gutiérrez, T. F. Heinz, S. S. Hong, J. Huang, A. F. Ismach, E. Johnston-Halperin, M. Kuno, V. V. Plashnitsa, R. D. Robinson, R. S. Ruoff, S. Salahuddin, J. Shan, L. Shi, M. G. Spencer, M. Terrones, W. Windl and J. E. Goldberger, *ACS Nano*, 2013, **7**, 2898–2926.

This journal is © the Owner Societies 2022

Phys. Chem. Chem. Phys., 2022, **24**, 28295–28305 | **28303**

21 M. Xu, T. Liang, M. Shi and H. Chen, *Chem. Rev.*, 2013, **113**, 3766–3798.

22 Z. Zhu, X. Cai, S. Yi, J. Chen, Y. Dai, C. Niu, Z. Guo, M. Xie, F. Liu, J. H. Cho, Y. Jia and Z. Zhang, *Phys. Rev. Lett.*, 2017, **119**, 106101.

23 J. Chen, Y. Dai, Y. Ma, X. Dai, W. Ho and M. Xie, *Nanoscale*, 2017, **9**, 15945–15948.

24 Y. Wang, G. Qiu, R. Wang, S. Huang, Q. Wang, Y. Liu, Y. Du, W. A. Goddard, M. J. Kim, X. Xu, P. D. Ye and W. Wu, *Nat. Electron.*, 2018, **1**, 228–236.

25 X. Huang, J. Guan, Z. Lin, B. Liu, S. Xing, W. Wang and J. Guo, *Nano Lett.*, 2017, **17**, 4619–4623.

26 J. Qin, G. Qiu, J. Jian, H. Zhou, L. Yang, A. Charnas, D. Y. Zemlyanov, C.-Y. Xu, X. Xu, W. Wu, H. Wang and P. D. Ye, *ACS Nano*, 2017, **11**, 10222–10229.

27 A. Apte, E. Bianco, A. Krishnamoorthy, S. Yazdi, R. Rao, N. Glavin, H. Kumazoe, V. Varshney, A. Roy, F. Shimojo, E. Ringe, R. K. Kalia, A. Nakano, C. S. Tiwary, P. Vashishta, V. Kochat and P. M. Ajayan, *2D Mater.*, 2018, **6**, 015013.

28 S. Yang, B. Chen, Y. Qin, Y. Zhou, L. Liu, M. Durso, H. Zhuang, Y. Shen and S. Tongay, *Phys. Rev. Lett.*, 2018, **2**, 104002.

29 D. Wang, A. Yang, T. Lan, C. Fan, J. Pan, Z. Liu, J. Chu, H. Yuan, X. Wang, M. Rong and N. Koratkar, *J. Mater. Chem. A*, 2019, **7**, 26326–26333.

30 Y. Liu, W. Wu and W. A. Goddard, *J. Am. Chem. Soc.*, 2018, **140**, 550–553.

31 J. Qiao, Y. Pan, F. Yang, C. Wang, Y. Chai and W. Ji, *Sci. Bull.*, 2018, **63**, 159–168.

32 S. Sharma, N. Singh and U. Schwingenschlögl, *ACS Appl. Energy Mater.*, 2018, **1**, 1950–1954.

33 J. Ma, F. Meng, J. He, Y. Jia and W. Li, *ACS Appl. Mater. Interfaces*, 2020, **12**, 43901–43910.

34 Y. C. Cheng, Z. Y. Zhu, M. Tahir and U. Schwingenschlögl, *EPL*, 2013, **102**, 57001.

35 A.-Y. Lu, H. Zhu, J. Xiao, C.-P. Chuu, Y. Han, M.-H. Chiu, C.-C. Cheng, C.-W. Yang, K.-H. Wei, Y. Yang, Y. Wang, D. Sokaras, D. Nordlund, P. Yang, D. A. Muller, M.-Y. Chou, X. Zhang and L.-J. Li, *Nat. Nanotechnol.*, 2017, **12**, 744–749.

36 J. Zhang, S. Jia, I. Kholmanov, L. Dong, D. Er, W. Chen, H. Guo, Z. Jin, V. B. Shenoy, L. Shi and J. Lou, *ACS Nano*, 2017, **11**, 8192–8198.

37 R. Li, Y. Cheng and W. Huang, *Small*, 2018, **14**, 1802091.

38 X. Yang, D. Singh, Z. Xu, Z. Wang and R. Ahuja, *J. Mater. Chem. C*, 2019, **7**, 12312–12320.

39 X. Yang, A. Banerjee and R. Ahuja, *ChemCatChem*, 2020, **12**, 6013–6023.

40 A. Rawat, M. K. Mohanta, N. Jena, Dimple, R. Ahammed and A. D. Sarkar, *J. Phys. Chem. C*, 2020, **124**, 10385–10397.

41 X. Yang, D. Singh, Z. Xu and R. Ahuja, *New J. Chem.*, 2020, **44**, 7932–7940.

42 S.-D. Guo, *Phys. Chem. Chem. Phys.*, 2018, **20**, 7236–7242.

43 S.-D. Guo, X.-S. Guo and Y. Deng, *J. Appl. Phys.*, 2019, **126**, 154301.

44 L. Cao, Y. S. Ang, Q. Wu and L. K. Ang, *Appl. Phys. Lett.*, 2019, **115**, 241601.

45 R. Gupta, B. Dongre, C. Bera and J. Carrete, *J. Phys. Chem. C*, 2020, **124**, 17476–17484.

46 A. Patel, D. Singh, Y. Sonvane, P. B. Thakor and R. Ahuja, *ACS Appl. Mater. Interfaces*, 2020, **12**, 46212–46219.

47 G. Kresse and D. Joubert, *Phys. Rev. B: Condens. Matter Mater. Phys.*, 1999, **59**, 1758–1775.

48 G. Kresse and J. Furthmüller, *Phys. Rev. B: Condens. Matter Mater. Phys.*, 1996, **54**, 11169–11186.

49 J. P. Perdew, K. Burke and M. Ernzerhof, *Phys. Rev. Lett.*, 1996, **77**, 3865–3868.

50 H. J. Monkhorst and J. D. Pack, *Phys. Rev. B: Solid State*, 1976, **13**, 5188–5192.

51 S. Grimme, *J. Comput. Chem.*, 2006, **27**, 1787–1799.

52 J. Heyd, G. E. Scuseria and M. Ernzerhof, *J. Chem. Phys.*, 2003, **118**, 8207–8215.

53 W. G. Hoover, *Phys. Rev. A: At., Mol., Opt. Phys.*, 1985, **31**, 1695–1697.

54 S. Nosé, *Mol. Phys.*, 1986, **57**, 187–191.

55 G. K. H. Madsen, J. Carrete and M. J. Verstraete, *Comput. Phys. Commun.*, 2018, **231**, 140–145.

56 A. Togo and I. Tanaka, *Scr. Mater.*, 2015, **108**, 1–5.

57 J. Carrete, B. Vermeersch, A. Katre, A. van Roekeghem, T. Wang, G. K. H. Madsen and N. Mingo, *Comput. Phys. Commun.*, 2017, **220**, 351–362.

58 V. B. Anzin, M. I. Eremets, Y. V. Kosichkin, A. I. Nadezhdinskii and A. M. Shirokov, *Phys. Status Solidi A*, 1977, **42**, 385–390.

59 J. Singh, M. Jakhar and A. Kumar, *Nanotechnology*, 2022, **33**, 215405.

60 H. Usui, K. Suzuki, K. Kuroki, S. Nakano, K. Kudo and M. Nohara, *Phys. Rev. B: Condens. Matter Mater. Phys.*, 2013, **88**, 075140.

61 K. Kuroki and R. Arita, *J. Phys. Soc. Jpn.*, 2007, **76**, 083707.

62 H. Usui and K. Kuroki, *J. Appl. Phys.*, 2017, **121**, 165101.

63 Y. Chen, J. Liu, J. Yu, Y. Guo and Q. Sun, *Phys. Chem. Chem. Phys.*, 2019, **21**, 1207–1216.

64 M. Cutler, J. F. Leavy and R. L. Fitzpatrick, *Phys. Rev.*, 1964, **133**, A1143–A1152.

65 G. D. Mahan and J. O. Sofo, *Proc. Natl. Acad. Sci. U. S. A.*, 1996, **93**, 7436–7439.

66 J. Qiao, X. Kong, Z.-X. Hu, F. Yang and W. Ji, *Nat. Commun.*, 2014, **5**, 4475.

67 G. J. Snyder and E. S. Toberer, *Nat. Mater.*, 2008, **7**, 105–114.

68 F. Q. Wang, S. Zhang, J. Yu and Q. Wang, *Nanoscale*, 2015, **7**, 15962–15970.

69 G. K. H. Madsen and D. J. Singh, *Comput. Phys. Commun.*, 2006, **175**, 67–71.

70 X. Wu, V. Varshney, J. Lee, Y. Pang, A. K. Roy and T. Luo, *Chem. Phys. Lett.*, 2017, **669**, 233–237.

71 P. Torres, F. X. Alvarez, X. Cartoixà and R. Rurali, *2D Mater.*, 2019, **6**, 035002.

72 B. Lv, X. Hu, N. Wang, J. Song, X. Liu and Z. Gao, *Appl. Surf. Sci.*, 2021, **559**, 149463.

73 N. Wang, H. Gong, Z. Sun, C. Shen, B. Li, H. Xiao, X. Zu, D. Tang, Z. Yin, X. Wu, H. Zhang and L. Qiao, *ACS Appl. Energy Mater.*, 2021, **4**, 12163–12176.

28304 | *Phys. Chem. Chem. Phys.*, 2022, **24**, 28295–28305

This journal is © the Owner Societies 2022

74 B. Peng, D. Zhang, H. Zhang, H. Shao, G. Ni, Y. Zhu and H. Zhu, *Nanoscale*, 2017, **9**, 7397–7407.

75 B. Peng, H. Zhang, H. Shao, Y. Xu, G. Ni, R. Zhang and H. Zhu, *Phys. Rev. B*, 2016, **94**, 245420.

76 B. Peng, H. Zhang, H. Shao, Y. Xu, X. Zhang and H. Zhu, *Ann. Phys.*, 2016, **528**, 504–511.

77 L. Lindsay, W. Li, J. Carrete, N. Mingo, D. A. Broido and T. L. Reinecke, *Phys. Rev. B: Condens. Matter Mater. Phys.*, 2014, **89**, 155426.

78 B. Peng, H. Zhang, H. Shao, Y. Xu, X. Zhang and H. Zhu, *Sci. Rep.*, 2016, **6**, 20225.

79 L.-D. Zhao, S.-H. Lo, Y. Zhang, H. Sun, G. Tan, C. Uher, C. Wolverton, V. P. Dravid and M. G. Kanatzidis, *Nature*, 2014, **508**, 373–377.

80 W. Li and N. Mingo, *Phys. Rev. B: Condens. Matter Mater. Phys.*, 2015, **91**, 144304.

81 Z. Gao, F. Tao and J. Ren, *Nanoscale*, 2018, **10**, 12997–13003.

This journal is © the Owner Societies 2022

Phys. Chem. Chem. Phys., 2022, **24**, 28295–28305 | **28305**